

RESEARCH ARTICLE

View Article Online
View Journal | View IssueCite this: *Mater. Chem. Front.*,
2022, 6, 2741

Achievement of high efficiency and thermally stable near-infrared phosphors by designing a chromium crystallographic environment for nondestructive testing and night vision†

Guohui Wei, Panlai Li, * Rui Li, Ye Wang, Hao Suo, Yuanbo Yang, Shaoxuan He, Jiehong Li, Yawei Shi and Zhijun Wang *

Clarification of the effect of the crystallographic environment of Cr³⁺ ions on its luminescence properties is essential for the construction of novel stable and efficient near-infrared (NIR) phosphors. To this end, we investigated a series of XTaO₄:Cr³⁺ (X = In, Sc, and Ga) phosphors with Cr³⁺ ions occupying the [XO₆] crystallographic sites. And the thermal stability increased from 8% to 73% and the IQE increased from 36% to 82.6% when X changed from In to Ga. An analysis of the internal reasons for the dramatic changes in the luminescence properties caused by Cr³⁺ ions occupying different crystallographic site environments has been performed in detail. With the order of X = In, Sc, and Ga, the Debye temperature of XTaO₄:Cr³⁺ was significantly enhanced and the electron–phonon coupling effect was gradually reduced, and as a result, GaTaO₄:Cr³⁺ with desirable structural rigidity has a high internal/external quantum efficiency (IQE/EQE: 82.6%/43.5%) and good thermal stability (*I*_{423K} = 73%). Finally, NIR phosphor-converted light-emitting diodes (pc-LEDs) were fabricated by combining XTaO₄:Cr³⁺ (X = In, Sc, and Ga) with blue LED chips and demonstrated for applications in nondestructive testing and night vision. The results provide a novel pointcut for the design of NIR light-emitting materials with desirable luminescence properties.

Received 14th June 2022,
Accepted 3rd August 2022

DOI: 10.1039/d2qm00569g

rsc.li/frontiers-materials

1 Introduction

NIR luminescent materials have generated significant interest in the biomedical field, nondestructive food testing, night vision, and bioimaging technologies.^{1–12} Compared to traditional NIR light sources such as halogen lamps and tungsten–halogen lamps, NIR pc-LEDs exhibit prominent advantages because of their low cost, high efficiency, and portability, which can be employed in a smart device.^{5,13–16} The Cr³⁺ ions with a 3d³ structure are the main protagonists of current NIR phosphor materials. First of all, their unique absorption band can be well adapted to the current blue-light and red-light chips. More importantly, Cr³⁺ doped NIR phosphors tend to exhibit high IQE and a relatively broad spectrum. Therefore, they have been more widely researched compared with other lanthanides (Nd³⁺, Pr³⁺, Yb³⁺, etc.)^{17,18} and transition metal elements (Mn²⁺, Ni²⁺, etc.).^{19–21}

Recently, crystal field engineering and co-doped rare-earth ions for energy transfer have been explored to optimize the luminescence performance of Cr³⁺-doped broadband NIR phosphors. In particular, modulating the crystal field environment by substitution of single cations or chemical units is an effective way to improve the luminescence performance, such as Sr(Al_{12–x}Ga_x)O₁₉:Cr³⁺, Gd₃(Sc_{2–x}Al_x)Ga₃O₁₂:Cr³⁺, Ca₃Hf₂(Lu_xAl_{2–x})SiO₁₂:Cr³⁺, and (Li_{1–x}In_{2–x}Zn_{2x})SbO₆:Cr³⁺.^{3,22–24} An enhancement of the luminescence properties can be achieved fundamentally by tuning the environment of the crystallographic site occupied by Cr³⁺ ions. However, currently, the research on the influence of the crystallographic sites occupied by Cr³⁺ ions on the luminescence properties (FWHM, thermal stability, and IQE) is still not comprehensive and remains a valuable and promising study.^{1,21–23,25–27} XTaO₄ (X = In, Sc, and Ga) is a layered structure with [XO₆] and [TaO₆] layers arranged in phase, which provides a relatively sensitive crystallographic sites environment for Cr³⁺ ions and can be used as a good host to study the effect of crystallographic sites environment on the luminescence properties of NIR phosphors. Recently, Zhang *et al.* reported a series of ABO₄:Cr³⁺ (A³⁺ = Ga, Sc, In, B⁵⁺ = Ta, Nb) NIR phosphors based on crystal site engineering and crystal field tuning, to achieve tunable photoluminescence.²⁸ From a different

Hebei Key Laboratory of Optic-Electronic Information and Materials,
College of Physics Science & Technology, Hebei University, Baoding 071002, China.
E-mail: li_panlai@126.com, wangzj1998@126.com

† Electronic supplementary information (ESI) available: Supporting Information is available from the author. See DOI: <https://doi.org/10.1039/d2qm00569g>

perspective, when we investigated the luminescence properties of $\text{XTaO}_4:\text{Cr}^{3+}$ ($X = \text{In}, \text{Sc}, \text{and Ga}$) phosphors, we found a phenomenon well worth exploring: the thermal stability increased from 8% to 73% and IQE increased from 36% to 82.6% when X changed from In to Ga. Such a large difference in luminescence properties may be closely related to the different crystallographic site environments for Cr^{3+} in $\text{XTaO}_4:\text{Cr}^{3+}$. Therefore, a detailed analysis of the internal reasons for the dramatic changes in luminescence properties caused by Cr^{3+} ions occupying different crystallographic site environments has been implemented, which will be helpful in exploring some fascinating properties of the matrix of NIR materials with excellent luminescence properties. The results showed that when $X = \text{Ga}$, that is $\text{GaTaO}_4:\text{Cr}^{3+}$, exhibited superior luminescence properties (IQE = 82.6%, EQE = 43.5%, $I_{423\text{K}} = 73\%$) due to its higher Debye temperature and lower electron–phonon coupling effect. And it was demonstrated that excellent structural rigidity and lower electron–phonon coupling effects are beneficial to enhancing the IQE/EQE and thermal stability of NIR phosphors, respectively. Finally, the NIR pc-LEDs were fabricated by combining commercial blue LED chips emitting at 450 nm with the prepared $\text{XTaO}_4:\text{Cr}^{3+}$ ($X = \text{In}, \text{Sc}, \text{and Ga}$) phosphors and demonstrated their promising applications in nondestructive testing and night vision.

2 Experimental sections

2.1 Materials and synthesis

Despite the inherent shortcomings of the high-temperature solid-state method (SSD), this method has the advantages of low cost, large yield, and a simple preparation process, and is widely used in commercial production of phosphor materials. And the high-temperature environment provided helps to improve the doping activator ions distributed homogeneously in the host lattice. In general, the emission intensity for a phosphor by SSD is higher than that by other methods. Furthermore, the composition of the host material XTaO_4 ($X = \text{Ga}, \text{Sc}, \text{and In}$) contains four kinds of cations, and the precursors cannot be selected easily for the sol–gel and precipitation processes, *etc.*, and the SSD seems to be the best choice. Therefore, all investigated phosphors were prepared *via* the SSD. The starting reagents Sc_2O_3 (99.99%), Ga_2O_3 (99.99%), In_2O_3 (99.99%), Ta_2O_5 (99.95%), and Cr_2O_3 (99.95%) were used as received without further purification. Stoichiometric amounts of raw materials weighed according to the nominal composition of $\text{X}_{1-x}\text{TaO}_4:x\text{Cr}^{3+}$ ($0 < x < 0.02$) were homogeneously mixed in an agate mortar and ground for 20 min. The obtained mixtures were then transferred into aluminum oxide crucibles and then sintered at 1500 °C for 10 h in air. After cooling, the samples were ground into powders for further measurement.

2.2 Characterization

The X-ray diffraction (XRD) patterns were tested by a Bruker D8 Advance X-ray diffractometer at 40 kV and 40 mA with $\text{Cu-}\alpha$ ($\lambda = 1.54056 \text{ \AA}$) irradiation. Rietveld refinement of the measured

XRD data was performed using GSAS software. X-Ray photoelectron spectra (XPS) were obtained using an X-ray photoelectron spectrometer, ThermoSphere ESCALAB 250Xi. The morphological characteristics of the prepared phosphors were recorded by field emission scanning electron microscopy (SEM, Nova Nano 450). The elemental composition and distribution were determined using an energy dispersive X-ray spectroscope attached to a SEM. The photoluminescence excitation (PLE) and photoluminescence emission (PL) spectra were recorded using a HORIBA FLuorolog3 fluorescence spectrometer with a 450 W Xe lamp as the excitation source low-temperature PL spectra were tested with an external device. The diffuse reflectance spectra (DRs) were measured on a Hitachi U4100, using BaSO_4 as a standard reference. The spectra TL were tested by an FJ-427A1 heat release meter to test the samples for heat release spectroscopy with a temperature rise rate of 1 K s^{-1} and a test range of 300–600 K.

2.3 Performance of LEDs

The NIR LED device is made of a synthetic NIR phosphor and a blue light chip with a power of 1 W and emission at 450 nm. The mass ratio of AB glue to NIR phosphor was set to 1 : 1 and mixed uniformly. The taken night vision pictures were obtained with the help of a NIR camera.

2.4 Density functional theory calculations (DFT)

DFT calculations were performed by Vienna *Ab Initio* Simulation Package (VASP). The projector augmented wave potential was implemented to describe the core electrons. The valence electrons were described by plane waves with a cutoff kinetic energy of 500 eV. The Brillouin zone was sampled in the Monkhorst–Pack scheme with a K -point. The convergence criteria of energy and forces were set as 10^{-5} eV and 0.05 eV \AA^{-1} , respectively. The electronica change-correlation energy was described by the generalized-gradient approximation of the Perdew–Burke–Ernzerhof (GGA-PBE) form.

3 Results and discussion

3.1 Structure and phase identification

Compounds with the general chemical formula XTaO_4 ($X = \text{In}, \text{Sc}, \text{and Ga}$) have been reported to adopt the monoclinic-type (P2/a). As displayed in Fig. 1a, the $2 \times 2 \times 2$ supercell of the XTaO_4 crystal structure is observed. The independent distribution of $[\text{XO}_6]$ and $[\text{TaO}_6]$ layers make these two octahedral environments very sensitive, and changes in their average bond length or cell volume can directly affect the rigidity of the structure. The phase purity of $\text{XTaO}_4:\text{Cr}^{3+}$ ($X = \text{In}, \text{Sc}, \text{and Ga}$) was checked by XRD (Fig. 1b). All the diffraction peaks can be well-matched with the standard card (GaTaO_4 : ICSD-#8128, ScTaO_4 : ICSD-#109192, GaTaO_4 : ICSD-#72569), indicating the successful synthesis of high-purity target phosphors. The XPS of XTaO_4 ($X = \text{In}, \text{Sc}, \text{and Ga}$) are presented in Fig. 1c. Binding energies corresponding to Ga-3s, Sc-2p, In-3d, Ta-4d, Cr-2p_{3/2}, and O-1s were detected in the XTaO_4 ($X = \text{In}, \text{Sc}, \text{and Ga}$), and

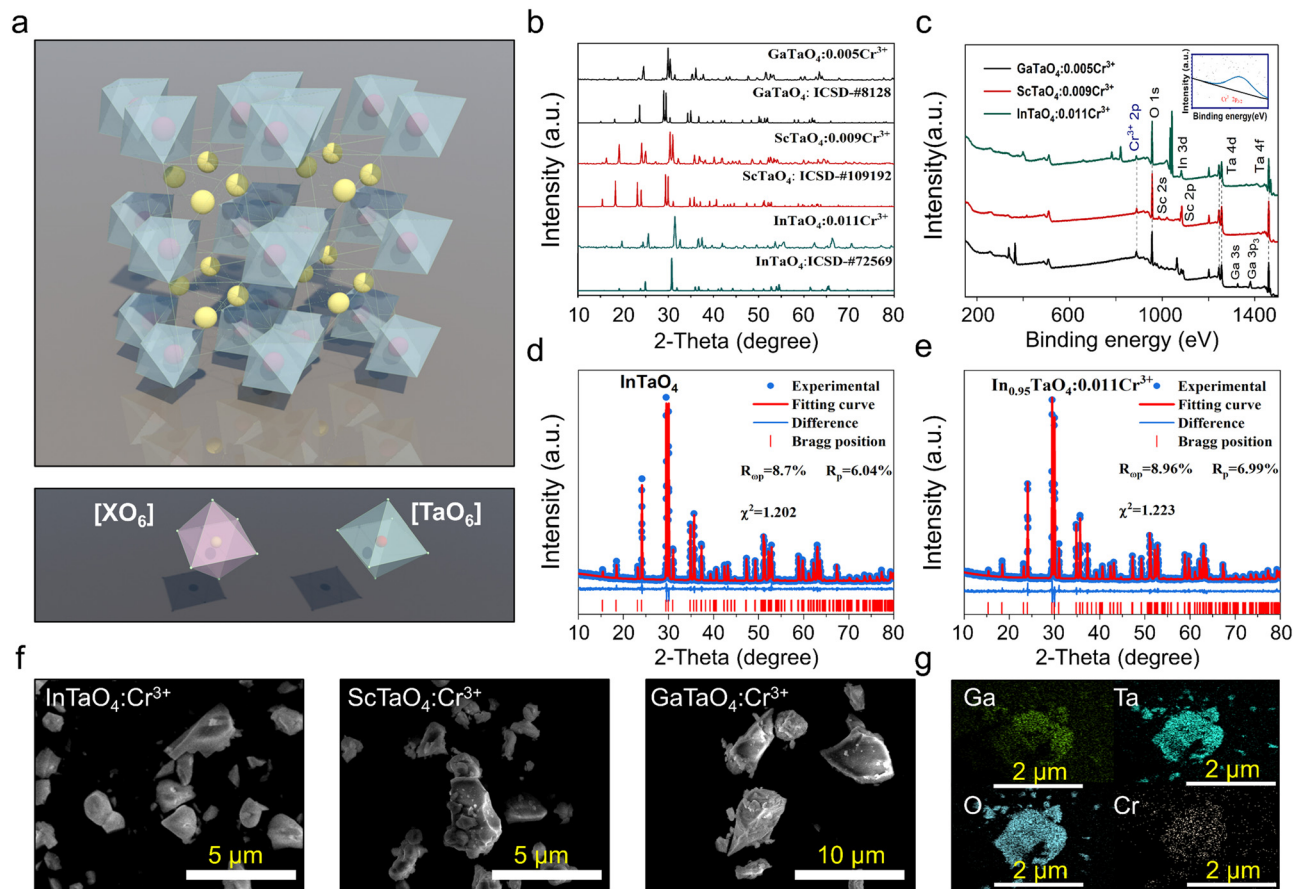


Fig. 1 (a) Crystal structure and the coordination environments of XTaO₄ (X = In, Sc, and Ga); (b) XRD patterns of XTaO₄ (X = In, Sc, and Ga); (c) XPS results of XTaO₄ (X = In, Sc, and Ga). The inset shows the binding energy peak of Cr³⁺-2p_{3/2}; (d and e) Rietveld refinement of XRD results of InTaO₄ and In_{0.989}TaO₄:0.011Cr³⁺; (f) SEM of XTaO₄:Cr³⁺ (X = In, Sc, and Ga); (g) mapping of GaTaO₄:Cr³⁺.

the binding energy peak of Cr-2p was weak due to the very low doping of Cr³⁺ relative to the host (the binding energy peak of 576.4 eV is magnified in the inset and corresponds to 2p_{3/2} of Cr³⁺). To further determine the crystal structure, the Rietveld refinement of the XRD data for the undoped and Cr³⁺-doped XTaO₄ (X = In, Sc, and Ga) sample is performed (Fig. 1d and e, detailed refinement data is placed in Tables S1 and S3, ESI†). The lattice parameters (*a*, *b*, and *c*) and volume (*V*) of the unit cell decrease with increasing Cr³⁺ concentration, while the refinement parameters remain essentially constant (Fig. S1, ESI†), which could prove that Cr³⁺ was effectively doped. The SEM images of XTaO₄ (X = In, Sc, and Ga) reveal that the size and morphology of the three sample particles are essentially uniform (Fig. 1f). The results of elemental mapping of XTaO₄:Cr³⁺ (X = In, Sc, and Ga) show that the elements Ga/Sc/In, Ta, Cr, and O are uniformly presented in the phosphor particles (Fig. 1g and Fig. S2 and S3, ESI†). The EDS results for XTaO₄:Cr³⁺ (X = In, Sc, and Ga) demonstrate the same elemental proportions as the molecular formula (Tables S4–S6, ESI†).

3.2 Luminescence properties of XTaO₄:Cr³⁺ (X = In, Sc, Ga)

The PLE spectra of XTaO₄:Cr³⁺ (X = In, Sc, and Ga) all have similar three excitation bands corresponding to the spin-allowed

transitions of Cr³⁺ (⁴A₂ → ⁴T₁ (⁴P), ⁴A₂ → ⁴T₁ (⁴F), and ⁴A₂ → ⁴T₂ (⁴F) transition). The three absorption bands of the diffuse reflectance spectra (DRS) of XTaO₄:Cr³⁺ (X = In, Sc, and Ga) can correspond well to the excitation spectra and have strong absorption bands in the range of 400–550 nm and 600–750 nm, which can match well with the emission bands of the blue and red chips (Fig. S4, ESI†). The XTaO₄:Cr³⁺ (X = In, Sc, and Ga) phosphors exhibit broadband NIR luminescence, which can be attributed to the spin-allowed ⁴T₂(⁴F) → ⁴A₂ transition of the octahedra occupied by the Cr³⁺ ion (Fig. 2a). For the lifetime tests of GaTaO₄:Cr³⁺ at different wavelengths at a low temperature of 4 K, there are only weak differences and it is difficult to distinguish multiple luminescence centers, so we tend to think that this is a single luminescence center formed by the Cr³⁺ ion occupying the [XO₆] octahedron (Fig. 2b and c). Furthermore, if the Cr³⁺ ion replaces the Ta⁵⁺ ion, it will lead to the substitution of charge imbalance and may form defects, but no defects were found by testing the thermoluminescence spectra (Fig. S5, ESI†). The use of DFT calculations in the GaTaO₄:Cr³⁺ system, as reported by Zhao *et al.* suggests that Cr³⁺ ions prefer to replace Ga³⁺ ions for luminescence.²⁹ To better illustrate this point, we added the relevant DFT calculation that the relative formation energy of the GaTaO₄ host is much smaller than that of the Ta⁵⁺ ion after its

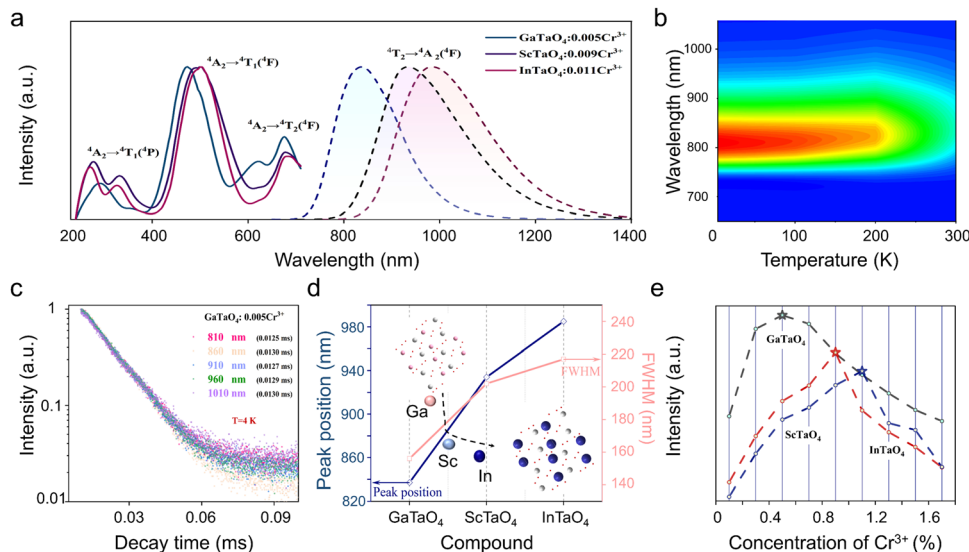


Fig. 2 (a) PLE and PL spectrum of $\text{XTaO}_4:\text{Cr}^{3+}$ ($X = \text{In, Sc, and Ga}$); (b) the low-temperature emission spectra of $\text{GaTaO}_4:\text{Cr}^{3+}$; (c) decay curves of $\text{GaTaO}_4:\text{Cr}^{3+}$ were monitored at 810 nm, 860 nm, 910 nm, 960 nm, and 1010 nm; (d) variation trend of the PL intensity of $\text{XTaO}_4:\text{Cr}^{3+}$ ($X = \text{In, Sc, and Ga}$) with Cr^{3+} -ion concentration; (e) the peaking position and FWHM of $\text{XTaO}_4:\text{Cr}^{3+}$ ($X = \text{In, Sc, and Ga}$).

substitution by the Cr^{3+} ion (Table S7, ESI†). This result suggests that Cr^{3+} is very much less inclined to occupy the Ta^{5+} ion. Meanwhile, the XRD of X^{3+} ions and Ta^{5+} ions substituted by Cr^{3+} ions were. The refinement parameters are smaller when X^{3+} ions are substituted by Cr^{3+} ions, which can be a good indication that Cr^{3+} ions prefer to substitute X^{3+} ions rather than Ta^{5+} ions (Fig. S6, ESI†). Having such a large difference in the luminescence properties is necessarily related to the sensitive $[\text{XO}_6]$ octahedral environment occupied by Cr^{3+} ions. As the average $\text{X}^{3+}-\text{O}^{2-}$ distance $d_{(\text{x-o})}$, octahedral volume $V_{[\text{XO}_6]}$ and luminescence peak positions in XTaO_4 ($X = \text{In, Sc, and Ga}$) generate a large variation ratio with the change of X^{3+} ion radius $r(\text{x})$ (Table 1). In contrast to $[\text{MO}_6]$ in $\text{Sr}_9\text{M}(\text{PO}_4)_7$ ($M = \text{Ga, Sc, In, and Lu}$) (where the $\text{X}^{3+}-\text{O}^{2-}$ average distance $d_{(\text{x-o})}$, octahedral volume $V_{[\text{XO}_6]}$, and luminescence peak position remain essentially constant as the M^{3+} ion radius changes),²⁵ $[\text{XO}_6]$ in XTaO_4 ($X = \text{In, Sc, and Ga}$) is a sensitive octahedron.

The lattice vibrational energy in the crystal is considered to be closely related to its structural rigidity, and to further illustrate the variation of structural rigidity; it can be evaluated theoretically by calculating the Debye temperature of XTaO_4 ($X = \text{In, Sc and Ga}$) using DFT with calculated values of 420.1 K, 430.801 K, and 488.329 K.^{6,30–32} As the structural rigidity of the crystallographic lattice environment occupied by Cr^{3+} ions changes, it makes XTaO_4 ($X = \text{In, Sc and Ga}$) show great differences in its luminescence properties.

Table 1 The ionic radii of X^{3+} ions, average $\text{X}^{3+}-\text{O}^{2-}$ distances, octahedral volumes $V_{[\text{XO}_6]}$, PL peak positions, and variation ratio for $\text{XTaO}_4:\text{Cr}^{3+}$ ($X = \text{Ga, Sc, and In}$)

Phosphor	$r(\text{x})$ (nm)	$d_{(\text{x-o})}$ (Å)	$V_{[\text{XO}_6]}$ (Å)	Peak (nm)
GaTaO_4	0.062	2.017	10.724	837
ScTaO_4	0.075	2.133	12.527	934
InTaO_4	0.08	2.151	12.861	985
Variation ratio (%)	29.03	6.64	19.93	17.7

In NIR phosphors with Cr^{3+} -doped octahedra, the emission wavelength depends mainly on the crystal field intensity of the phosphor. When the X^{3+} ions are Ga^{3+} , Sc^{3+} , and In^{3+} in that order, respectively, the crystal field intensity decreases from 2.29 to 2.03 as calculated from the crystal field equation, which indicates that $\text{XTaO}_4:\text{Cr}^{3+}$ ($X = \text{Ga, Sc, and In}$) is located in the weak crystal field. When the Dq/B value decreases, it leads to a gradual decrease in the energy level difference between the ${}^4\text{T}_2$ and ${}^4\text{A}_2$ levels, (Fig. S7, ESI†), which is the main reason for the redshift of the peak position from 837 nm to 985 nm.²⁷ The FWHM broadens from Ga^{3+} (156 nm) to In^{3+} (217 nm), which is determined by the electron–phonon coupling effect (Fig. 2d).^{27,33} When the X^{3+} ions are Ga^{3+} , Sc^{3+} , and In^{3+} in order, the $\text{X}^{3+}-\text{O}^{2-}$ bond stretching increases, the $[\text{XO}_6]$ octahedral lattice expands, and the gradually expanding coordination environment leads to a larger Stokes shift, because the Stokes shift is strongly influenced by the rigidity of the crystal structure. Therefore, the non-radiative transitions generated when the X^{3+} ion is Ga^{3+} will be weaker than that for Sc^{3+} and In^{3+} , and the emission intensity of $\text{GaTaO}_4:\text{Cr}^{3+}$ will be stronger (Fig. 2e and Fig. S8, ESI†).^{26,33,34}

Meanwhile, the IQE of the phosphor is an important parameter to evaluate whether it can be used as an efficient phosphor for pc-LED. The IQE values of $\text{XTaO}_4:\text{Cr}^{3+}$ ($X = \text{In, Sc, and Ga}$) were 36%, 54%, and 82.6%, respectively (Fig. S9, ESI†), where $\text{GaTaO}_4:\text{Cr}^{3+}$ was superior to most of the previously reported Cr^{3+} -doped NIR phosphors (Table 2). Excellent structural rigidity has been reported to be effective in enhancing photon emission and enhancing IQE.^{35,36} Since $[\text{XO}_6]$ is a sensitive octahedral structure, the change of X^{3+} ions will have a great impact on the structural rigidity. When the X^{3+} ion changes from the Ga^{3+} ion to the In^{3+} ion, the structure will become loose, allowing the soft phonon mode of nonradiative relaxation to be enhanced, thus increasing the tendency for photon emission and causing a substantial decrease in IQE.³⁶

Table 2 Summary of some of the reported luminescent properties of NIR phosphors

Phosphor	λ_{em} (nm)	FWHM (nm)	IQE/EQE (%)	I_{423K} (%)	Ref.
$\text{La}_2\text{MgZrO}_6:\text{Cr}^{3+}$	825	210	58/-	40	14
$\text{Ca}_2\text{LuZr}_2\text{Al}_3\text{O}_{12}:\text{Cr}^{3+}$	752	117	69/-	60	37
$\text{La}_3\text{Sc}_2\text{Ga}_3\text{O}_{12}:\text{Cr}^{3+}$	818	145	35/-	60	33
$\text{ScBO}_3:\text{Cr}^{3+}$	800	120	65/-	51	38
$\text{Na}_3\text{In}_2\text{Li}_3\text{F}_{12}:\text{Cr}^{3+}$	778	121	87.2/20.05	58	18
$\text{ScF}_3:\text{Cr}^{3+}$	853	140	45/-	85.5	4
$\text{MgAl}_2\text{O}_4:\text{Cr}^{3+}$	740	140	15/-	59	5
$\text{LiScP}_2\text{O}_7:\text{Cr}^{3+}$	880	170	53/-	18	39
$\text{GaTaO}_4:\text{Cr}^{3+}$	850	266	82.6/43.5	73	This work

3.3 Temperature-dependent spectra analysis

To analyze the thermal stability of XTaO_4 ($X = \text{In, Sc, and Ga}$), PL spectra in the temperature range of 273–473 K were tested (Fig. 3a and Fig. S10, ESI†). The temperature-dependent normalized spectrum of $\text{GaTaO}_4:\text{Cr}^{3+}$ is redshifted by about 19 nm and the FWHM broadens from 155 nm to 174 nm. The redshift at the peak position comes from the temperature-induced weakening of the crystal field environment, while the broadening of the emission peak is due to the enhancement of the electron–phonon coupling effect (Fig. 3b). Here the enhancement of the electron–phonon coupling effect is

reflected by the Huang–Rhys factor (S), the resulting S and $\hbar\omega$ of $\text{XTaO}_4:\text{Cr}^{3+}$ ($X = \text{Ga, Sc, and In}$) are calculated to be 1.4 and 50.45 meV, 3.11 and 33 meV, 5.26 and 12.45 meV (the detailed calculation procedure is placed in the ESI† ‘Measurements of Huang–Rhys factor’ and Fig. S11, ESI†). In general, the Stokes displacement and FWHM increase as the S value increases, which will lead to weaker thermal stability. The integrated emission intensity of $\text{XTaO}_4:\text{Cr}^{3+}$ ($X = \text{In, Sc, and Ga}$) at 423 K remains around 8%, 12%, and 73% of the room temperature value, respectively (Fig. 3c). Compared with the other reported broadband NIR phosphors listed in Table 2, the thermal stability of $\text{GaTaO}_4:\text{Cr}^{3+}$ is competitive.

To better understand the luminescence thermal stability, the activation energy (E_a) can be calculated by the Arrhenius equation:^{19,33,37}

$$\ln\left(\frac{I_0}{I_T}\right) = \ln A - \frac{E_a}{k_B} \quad (1)$$

where I_0 is the initial emission intensity at 273 K, I_T is the emission intensity at a given temperature T , A is constant, and k_B is the Boltzmann constant ($8.617 \times 10^{-5} \text{ eV K}^{-1}$). The energy difference between the lowest excited state and intersection point is defined as the thermal activation energy E_a , which can be estimated to be 0.440 eV, 0.443 eV, and 0.502 eV for the composition of $\text{XTaO}_4:\text{Cr}^{3+}$ ($X = \text{In, Sc, and Ga}$), respectively. The thermal

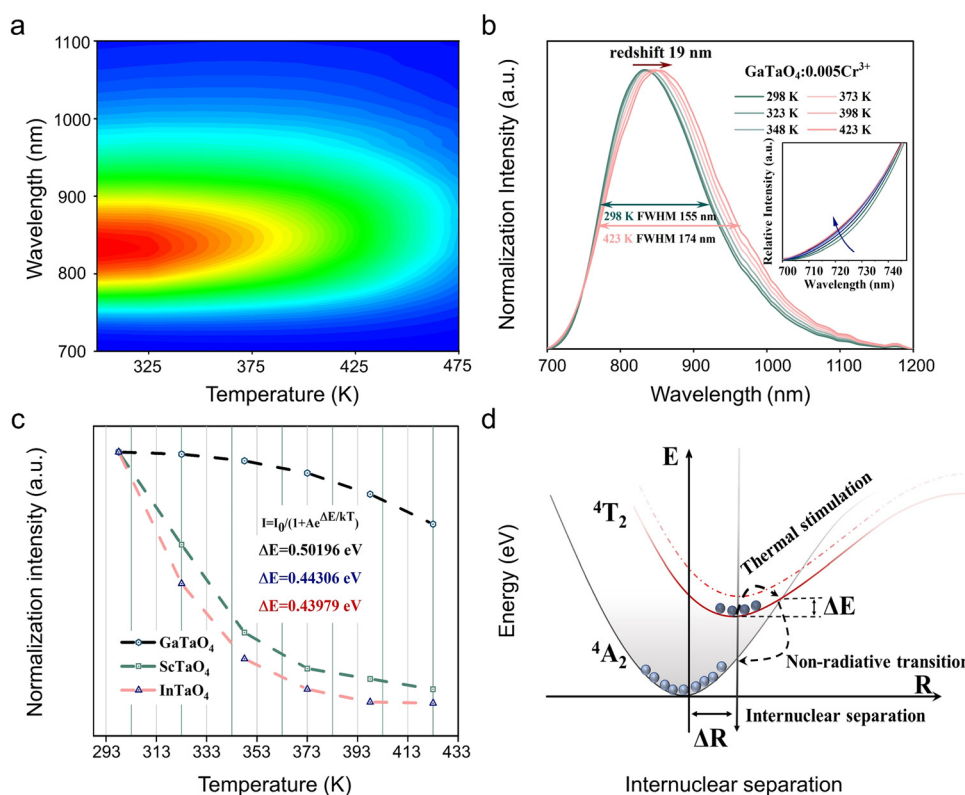


Fig. 3 (a) Temperature-dependent PL spectra of samples $\text{GaTaO}_4:0.005\text{Cr}^{3+}$; (b) temperature-dependent PL spectra of the normalized intensities for the $\text{GaTaO}_4:0.005\text{Cr}^{3+}$ sample, and the inset represents the emission spectra wavelength from 700 nm to 750 nm; (c) The integrated intensities of temperature-dependent NIR emission of $\text{XTaO}_4:\text{Cr}^{3+}$ ($X = \text{In, Sc, and Ga}$); the values are the fitting results for the Arrhenius equation; (d) configuration coordinate diagram of Cr^{3+} -ions in the $\text{XTaO}_4:\text{Cr}^{3+}$ ($X = \text{In, Sc, and Ga}$) host.

quenching process can be described in Fig. 3d *via* a configurational coordinate diagram. When the activation energy ΔE increases, it is more difficult for the activated electrons to overcome the energy barrier ΔE , so the nonradiative transition decreases, leading to an increase in thermal stability. Such a huge difference in thermal stability performance is triggered by two main points: first, the X^{3+} ions in the sequence of Ga^{3+} , Sc^{3+} , and In^{3+} provide a gradually relaxing luminescent environment for the Cr^{3+} ions, leading to an enhanced electron–phonon coupling effect, which makes the cross-relaxation between the phonon-assisted excited and ground states easier. Second, the doping of Cr^{3+} ions in the sensitive $[XO_6]$ octahedral lattice sites, with the X^{3+} ions being Ga^{3+} , Sc^{3+} , and In^{3+} in sequence, the progressively relaxed environment of the octahedra leads to an increase in the Stokes shift as well as a decrease in the activation energy ΔE , allowing the probability of the nonradiative transition to be increased, resulting in a lower thermal quenching resistance.

3.4 NIR pc-LED application

Given the excellent luminescence properties of $XTaO_4:Cr^{3+}$ ($X = In, Sc, Ga$) phosphors, NIR pc-LED were prepared by combining commercial InGaN chips. The NIR output power of $XTaO_4:Cr^{3+}$ ($X = In, Sc, and Ga$) was 282 mW, 283 mW, and 287 mW, respectively, while the efficiency was 0.7%, 1.9%, and 11.5%, respectively, when the driving current was 100 mA

(Fig. 4a). Among them, $GaTaO_4:Cr^{3+}$ has better luminescence properties, and its photoelectric conversion efficiency decreases from 11.5% to 3.9% (as the current thermal effect, with the increase of current, causes a certain amount of energy to be dissipated as a thermal energy situation, resulting in the decrease of photoelectric conversion efficiency) and output power increases from 287 mW to 4090 mW when the driving current is from 100 mA to 1000 mA (Fig. 4b). It is worth noting that the actual output power should be higher since the detector can only effectively capture the energy that is certain to pass under the NIR emission range (650–1000 nm). In addition, the operating temperature of the high-power pc-LED increases from about 300 K to about 420 K when the drive current increases from 0 mA to 800 mA (Fig. 4c), demonstrating that the fabricated $XTaO_4:Cr^{3+}$ ($X = In, Sc, and Ga$) NIR pc-LEDs still exhibit good luminescence performance in practical applications.

The application of the NIR pc-LED of $GaTaO_4:Cr^{3+}$ in night vision is demonstrated in Fig. 5a. For NIR spectroscopy applications, the ideal light source should have a broad spectrum to cover more information about the functional groups. Herein, the spectral luminescence spectra of $XTaO_4:Cr^{3+}$ ($X = In, Sc, and Ga$) in the bands 700–1200, 800–1300, 850–1400 nm respectively can be combined to detect more information in the ultra-wide range. The PL spectra of five solutions (water, glucose, tea, milk, and coffee) after penetrating them with three LEDs respectively are

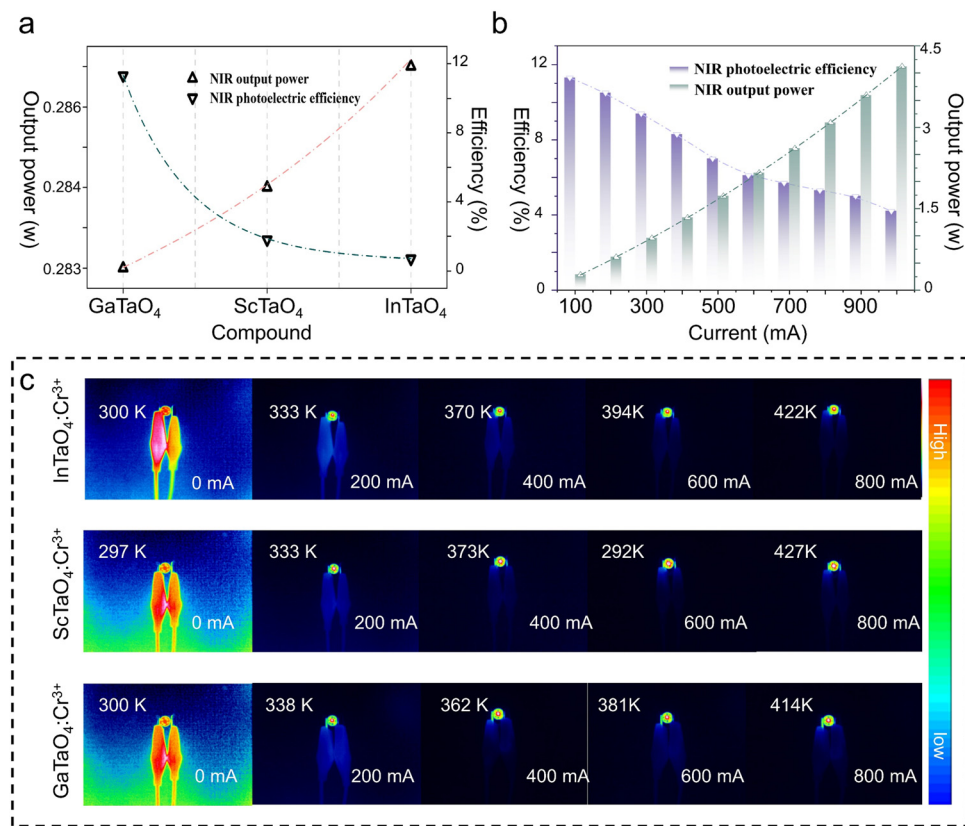


Fig. 4 (a) Output optical powers, and conversion efficiencies of the NIR-LED of $XTaO_4:Cr^{3+}$ ($X = In, Sc, and Ga$) depending on the 100 mA driving current; (b) output optical powers, and conversion efficiencies of the NIR-LED of $GaTaO_4:Cr^{3+}$ depending on the driving current from 100 mA to 1000 mA; (c) thermal images of the pc-LED of $XTaO_4:Cr^{3+}$ ($X = In, Sc, and Ga$) at different operating currents over 0–800 mA.

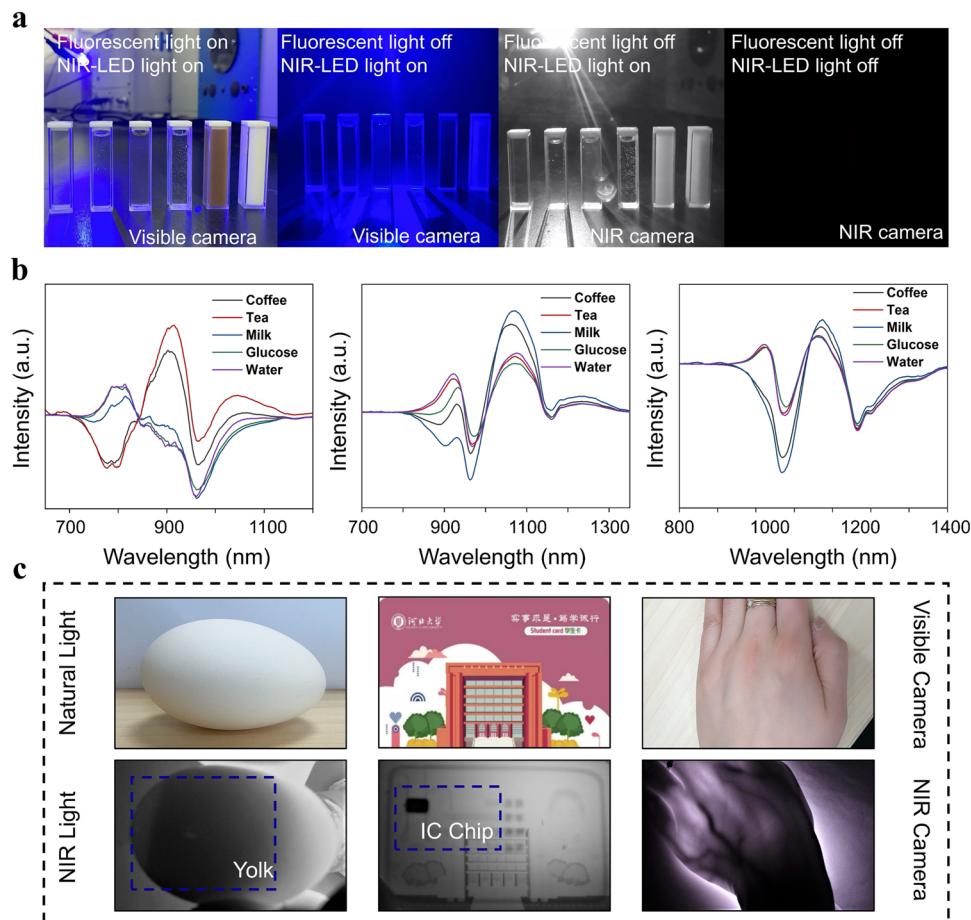


Fig. 5 A multitude of applications of $\text{XTaO}_4:\text{Cr}^{3+}$ ($X = \text{In}, \text{Sc}, \text{and Ga}$) are demonstrated; (a) night vision (visual and NIR images of water, glucose, tea, milk, and coffee); (b) nondestructive food detection (NIR spectra after penetrating water, glucose, tea, milk, and coffee); (c) NIR non-destructive testing applications (photos of eggs, access cards and palms in natural and NIR light).

shown in Fig. S12 (ESI[†]). Using the spectrum without penetrating any substance as the normal line, the difference spectrum can distinguish the five solutions more clearly (Fig. 5b). It was found that the solution has different absorption in the 700–1400 nm range and the light sources with different peak wavelengths show different detection sensitivity to the absorption signal, which is very obvious in the case of milk. The combination of the three LEDs gives more complete information on the absorption of each sample, which can improve the accuracy of monitoring, demonstrating their potential for non-destructive testing applications. Finally, the ability to compare images of eggs, access cards, and palms took in both natural and NIR light demonstrates the viability of nondestructive inspection using $\text{GaTaO}_4:\text{Cr}^{3+}$ manufactured NIR pc-LED in a variety of working circumstances (Fig. 5c). In summary, NIR pc LED-based non-destructive testing may become an effective and convenient alternative to traditional radiography.

4 Conclusions

In summary, it was demonstrated *via* Debye temperature, electron–phonon coupling effects, and crystal field theory that

the structural rigidity of $\text{XTaO}_4:\text{Cr}^{3+}$ ($X = \text{In}, \text{Sc}, \text{and Ga}$) becomes progressively stronger when the X^{3+} ions are In^{3+} , Sc^{3+} and Ga^{3+} ions in sequence, leading to a significant improvement in the luminescence properties (thermal stability: In^{3+} (8%) \rightarrow Ga^{3+} (73%), IQE: In^{3+} (36%) \rightarrow Ga^{3+} (82.6%)). The rigid structure will effectively enhance the luminescence properties of Cr^{3+} ions, and the detailed mechanism explanation provides an effective idea to continue the exploration of novel stable and efficient NIR phosphors in the future. Due to its excellent rigidity, $\text{GaTaO}_4:\text{Cr}^{3+}$ has excellent IQE/EQE (82.6%/43.5%) and good thermal stability ($I_{423\text{K}} = 73\%$), which meets the current requirements for high-performance NIR phosphors. Ultimately, a series of $\text{XTaO}_4:\text{Cr}^{3+}$ ($X = \text{In}, \text{Sc}, \text{and Ga}$) NIR pc-LED devices were fabricated, proving their promising applications in night vision, food composition analysis, and non-destructive testing.

Conflicts of interest

The authors declare no conflict of interest.

Acknowledgements

The work is supported by the National Natural Science Foundation of China (No. 51902080), the Natural Science Foundation of Hebei Province, China (No. E2019201223), the personnel training project of Hebei Province, China (No. A201902005), and the central government to guide local scientific and Technological Development (No. 206Z1102G and 216Z1101G).

References

- Z. Wu, X. Han, Y. Zhou, K. Xing, S. Cao, L. Chen, R. Zeng, J. Zhao and B. Zou, Efficient broadband near-infrared luminescence of Cr³⁺ doped fluoride K₂NaInF₆ and its NIR-LED application toward veins imaging, *Chem. Eng. J.*, 2022, **427**, 131740.
- H. Yu, J. Chen, R. Mi, J. Yang and Y. Liu, Broadband near-infrared emission of K₃ScF₆:Cr³⁺ phosphors for night vision imaging system sources, *Chem. Eng. J.*, 2021, **417**, 129271.
- Y. Wei, P. Dang, Z. Dai, G. Li and J. Lin, Advances in Near-Infrared Luminescent Materials without Cr³⁺: Crystal Structure Design, Luminescence Properties, and Applications, *Chem. Mater.*, 2021, **33**(14), 5496–5526.
- Q. Lin, Q. Wang, M. Liao, M. Xiong, X. Feng, X. Zhang, H. Dong, D. Zhu, F. Wu and Z. Mu, Trivalent Chromium Ions Doped Fluorides with Both Broad Emission Bandwidth and Excellent Luminescence Thermal Stability, *ACS Appl. Mater. Interfaces*, 2021, **13**(15), 18274–18282.
- J. Qiao, G. Zhou, Y. Zhou, Q. Zhang and Z. Xia, Divalent europium-doped near-infrared-emitting phosphor for light-emitting diodes, *Nat. Commun.*, 2019, **10**(1), 5267.
- C. Yuan, R. Li, Y. Liu, L. Zhang, J. Zhang, G. Leniec, P. Sun, Z. Liu, Z. Luo, R. Dong and J. Jiang, Efficient and Broadband LiGaP₂O₇:Cr³⁺ Phosphors for Smart Near-Infrared Light-Emitting Diodes, *Laser Photonics Rev.*, 2021, 2100227.
- F. He, E. Song, Y. Zhou, H. Ming, Z. Chen, J. Wu, P. Shao, X. Yang, Z. Xia and Q. Zhang, A General Ammonium Salt Assisted Synthesis Strategy for Cr³⁺-Doped Hexafluorides with Highly Efficient Near-Infrared Emissions, *Adv. Funct. Mater.*, 2021, **31**(36), 2103743.
- D. Liu, G. Li, P. Dang, Q. Zhang, Y. Wei, H. Lian, M. Shang, C. C. Lin and J. Lin, Simultaneous Broadening and Enhancement of Cr³⁺ Photoluminescence in LiIn₂SbO₆ by Chemical Unit Co substitution: Night-Vision and Near-Infrared Spectroscopy Detection Applications, *Angew. Chem., Int. Ed.*, 2021, **60**(26), 14644–14649.
- C. Dincer, R. Bruch, E. Costa-Rama, M. T. Fernandez-Abedul, A. Merkoci, A. Manz, G. A. Urban and F. Guder, Disposable Sensors in Diagnostics, Food, and Environmental Monitoring, *Adv. Mater.*, 2019, **31**(30), e1806739.
- Y. J. Liang, F. Liu, Y. F. Chen, X. J. Wang, K. N. Sun and Z. Pan, New function of the Yb³⁺ ion as an efficient emitter of persistent luminescence in the short-wave infrared, *Light: Sci. Appl.*, 2016, **5**(7), e16124.
- K. Tuong Ly, R.-W. Chen-Cheng, H.-W. Lin, Y.-J. Shiau, S.-H. Liu, P.-T. Chou, C.-S. Tsao, Y.-C. Huang and Y. Chi, Near-infrared organic light-emitting diodes with very high external quantum efficiency and radiance, *Nat. Photonics*, 2016, **11**(1), 63–68.
- Y. Gu, Z. Guo, W. Yuan, M. Kong, Y. Liu, Y. Liu, Y. Gao, W. Feng, F. Wang, J. Zhou, D. Jin and F. Li, High-sensitivity imaging of time-domain near-infrared light transducer, *Nat. Photonics*, 2019, **13**(8), 525–531.
- W. T. Huang, C. L. Cheng, Z. Bao, C. W. Yang, K. M. Lu, C. Y. Kang, C. M. Lin and R. S. Liu, Broadband Cr³⁺, Sn⁴⁺-Doped Oxide Nanophosphors for Infrared Mini Light-Emitting Diodes, *Angew. Chem., Int. Ed.*, 2019, **58**(7), 2069–2072.
- H. Zeng, T. Zhou, L. Wang and R.-J. Xie, Two-Site Occupation for Exploring Ultra-Broadband Near-Infrared Phosphor-Double-Perovskite La₂MgZrO₆:Cr³⁺, *Chem. Mater.*, 2019, **31**(14), 5245–5253.
- P. Xiong, M. Peng, K. Qin, F. Xu and X. Xu, Visible to Near-Infrared Persistent Luminescence and Mechanoluminescence from Pr³⁺-Doped LiGa₅O₈ for Energy Storage and Bioimaging, *Adv. Opt. Mater.*, 2019, **7**(24), 1901107.
- J. Cao, J. Peng, L. Wang, H. Luo, X. Wang, P. Xiong, Y. Wang and M. Peng, Broadband NIR emission from multiple Bi centers in nitridated borogermanate glasses via tailoring local glass structure, *J. Mater. Chem. C*, 2019, **7**(7), 2076–2084.
- X. Zhou, W. Geng, J. Li, Y. Wang, J. Ding and Y. Wang, An Ultraviolet-Visible and Near-Infrared-Responded Broadband NIR Phosphor and Its NIR Spectroscopy Application, *Adv. Opt. Mater.*, 2020, **8**(8), 1902003.
- S. He, L. Zhang, H. Wu, H. Wu, G. Pan, Z. Hao, X. Zhang, L. Zhang, H. Zhang and J. Zhang, Efficient Super Broadband NIR Ca₂LuZr₂Al₃O₁₂:Cr³⁺, Yb³⁺ Garnet Phosphor for pc-LED Light Source toward NIR Spectroscopy Applications, *Adv. Opt. Mater.*, 2020, **8**(6), 1901684.
- M. Northey and J. Mckibbin, Optical Spectroscopy of Inorganic Solids, *Monogr. Phys. Chem. Mater.*, 2006, 45–59.
- T. Maldiney, A. Bessière, J. Seguin, E. Teston, S. K. Sharma, B. Viana, A. J. J. Bos, P. Dorenbos, M. Besides, D. Gourier, D. Scherman and C. Richard, The in vivo activation of persistent nanophosphors for optical imaging of vascularization, tumors, and grafted cells, *Nat. Mater.*, 2014, **13**(4), 418–426.
- Z. Pan, Y. Y. Lu and F. Liu, Sunlight-activated long-persistent luminescence in the near-infrared from Cr³⁺-doped zinc gallogermanates, *Nat. Mater.*, 2011, **11**(1), 58–63.
- V. Rajendran, M. H. Fang, W. T. Huang, N. Majewska, T. Lesniewski, S. Mahlik, G. Lennie, S. M. Kaczmarek, W. K. Pang, V. K. Peterson, K. M. Lu, H. Chang and R. S. Liu, Chromium Ion Pair Luminescence: A Strategy in Broadband Near-Infrared Light-Emitting Diode Design, *J. Am. Chem. Soc.*, 2021, **143**(45), 19058–19066.
- E. T. Basore, W. Xiao, X. Liu, J. Wu and J. Qiu, Broadband Near-Infrared Garnet Phosphors with Near-Unity Internal Quantum Efficiency, *Adv. Opt. Mater.*, 2020, **8**(12), 2000296.
- L. Zhang, D. Wang, Z. Hao, X. Zhang, G. H. Pan, H. Wu and J. Zhang, Cr³⁺-Doped Broadband NIR Garnet Phosphor with

- Enhanced Luminescence and its Application in NIR Spectroscopy, *Adv. Opt. Mater.*, 2019, 7(12), 1900185.
- 25 F. Zhao, H. Cai, Z. Song and Q. Liu, Structural Confinement for Cr³⁺ Activators toward Efficient Near-Infrared Phosphors with Suppressed Concentration Quenching, *Chem. Mater.*, 2021, 33(10), 3621–3630.
- 26 F. Y. Zhao, H. Cai, S. Y. Zhang, Z. Song and Q. L. Liu, Octahedron-dependent near-infrared luminescence in Cr³⁺-activated phosphors, *Mater. Today Chem.*, 2022, 23, 100704.
- 27 W. Nie, Y. Li, J. Zuo, Y. Kong, W. Zou, G. Chen, J. Peng, F. Du, L. Han and X. Ye, Cr³⁺-activated Na₃X₂Li₃F₁₂ (X = Al, Ga, or In) garnet phosphors with broadband NIR emission and high luminescence efficiency for potential biomedical application, *J. Mater. Chem. C*, 2021, 9(42), 15230–15241.
- 28 Q. Zhang, D. Liu, P. Dang, H. Lian, G. Li and J. Lin, Two Selective Sites Control of Cr³⁺-Doped ABO₄ Phosphors for Tuning Ultra-Broadband Near-Infrared Photoluminescence and Multi-Applications, *Laser Photonics Rev.*, 2021, 16(2), 2100459.
- 29 J. Zhong, Y. Zhuo, F. Du, H. Zhang, W. Zhao, S. You and J. Brgoch, Efficient Broadband Near-Infrared Emission in the GaTaO₄:Cr³⁺ Phosphor, *Adv. Opt. Mater.*, 2021, 10(2), 2101800.
- 30 X. Xu, Q. Shao, L. Yao, Y. Dong and J. Jiang, Highly efficient and thermally stable Cr³⁺-activated silicate phosphors for broadband near-infrared LED applications, *Chem. Eng. J.*, 2020, 383, 123108.
- 31 M.-H. Fang, G. N. A. De Guzman, Z. Bao, N. Majewska, S. Mahlik, M. Grinberg, G. Leniec, S. M. Kaczmarek, C.-W. Yang, K.-M. Lu, H.-S. Sheu, S.-F. Hu and R.-S. Liu, Ultra-high-efficiency near-infrared Ga₂O₃:Cr³⁺ phosphor and controlling of phytochrome, *J. Mater. Chem. C*, 2020, 8(32), 11013–11017.
- 32 L. You, R. Tian, T. Zhou and R.-J. Xie, Broadband near-infrared phosphor BaMgAl₁₀O₁₇:Cr³⁺ realized by crystallographic site engineering, *Chem. Eng. J.*, 2021, 417, 129224.
- 33 B. Malysa, A. Meijerink and T. Jüstel, Temperature-dependent Cr³⁺ photoluminescence in garnets of the type X₃Sc₂Ga₃O₁₂ (X = Lu, Y, Gd, La), *J. Lumin.*, 2018, 202, 523–531.
- 34 L. He, Z. Song, X. Jia, Z. Xia and Q. Liu, Consequence of Optimal Bonding on Disordered Structure and Improved Luminescence Properties in T-Phase (Ba, Ca)₂SiO₄:Eu⁽²⁺⁾ Phosphor, *Inorg. Chem.*, 2018, 57(7), 4146–4154.
- 35 J. Brgoch, S. P. DenBaars and R. Seshadri, Proxies from Ab Initio Calculations for Screening Efficient Ce³⁺ Phosphor Hosts, *J. Phys. Chem. C*, 2013, 117(35), 17955–17959.
- 36 Y. Zhuo, A. Mansouri Tehrani, A. O. Olynyk, A. C. Duke and J. Brgoch, Identifying an efficient, thermally robust inorganic phosphor host via machine learning, *Nat. Commun.*, 2018, 9(1), 4377.
- 37 L. Zhang, S. Zhang, Z. Hao, X. Zhang, G.-H. Pan, Y. Luo, H. Wu and J. Zhang, A high-efficiency broadband near-infrared Ca₂LuZr₂Al₃O₁₂:Cr³⁺ garnet phosphor for blue LED chips, *J. Mater. Chem. C*, 2018, 6(18), 4967–4976.
- 38 M.-H. Fang, P.-Y. Huang, Z. Bao, N. Majewska, T. Leśniewski, S. Mahlik, M. Grinberg, G. Leniec, S. M. Kaczmarek, C.-W. Yang, K.-M. Lu, H.-S. Sheu and R.-S. Liu, Penetrating Biological Tissue Using Light-Emitting Diodes with a Highly Efficient Near-Infrared ScBO₃:Cr³⁺ Phosphor, *Chem. Mater.*, 2020, 32(5), 2166–2171.
- 39 L. Yao, Q. Shao, S. Han, C. Liang, J. He and J. Jiang, Enhancing Near-Infrared Photoluminescence Intensity and Spectral Properties in Yb³⁺ Codoped LiScP₂O₇:Cr³⁺, *Chem. Mater.*, 2020, 32(6), 2430–2439.